Path integral Liouville dynamics: Applications to infrared spectra of OH, water, ammonia, and methane

Jian Liu (iD), and Zhijun Zhang (iD)

View Online

Export Citation

CrossMark

ARTICLES YOU MAY BE INTERESTED IN

AIP Publishing

Path integral Liouville dynamics: Applications to infrared spectra of OH, water, ammonia, and methane

Jian Liu[1,2,a)] and Zhijun Zhang[1]

[1]*Beijing National Laboratory for Molecular Sciences, Institute of Theoretical and Computational Chemistry, College of Chemistry and Molecular Engineering, Peking University, Beijing 100871, China*
[2]*State Key Joint Laboratory of Environmental Simulation and Pollution Control, College of Environmental Sciences and Engineering, Peking University, Beijing 100871, China*

Path integral Liouville dynamics (PILD) is applied to vibrational dynamics of several simple but representative realistic molecular systems (OH, water, ammonia, and methane). The dipole-derivative autocorrelation function is employed to obtain the infrared spectrum as a function of temperature and isotopic substitution. Comparison to the exact vibrational frequency shows that PILD produces a reasonably accurate peak position with a relatively small full width at half maximum. PILD offers a potentially useful trajectory-based quantum dynamics approach to compute vibrational spectra of molecular systems. © 2016 AIP Publishing LLC. [http://dx.doi.org/10.1063/1.4939953]

I. INTRODUCTION

Normal-mode analysis of the equilibrium configuration (structure) is a standard tool to calculate vibrational frequencies and the corresponding collective motions of molecules in the harmonic approximation.[1] When anharmonicity becomes strong in the potential energy surface (PES), normal-mode frequencies are often significantly deviated from exact results. For instance, the normal-mode frequency of the Morse potential for OH is blue-shifted (by about 180 cm^{-1}) from the exact result.[2,3]

The correlation function offers another approach to obtain vibrational frequencies. For example, the infrared (IR) spectrum is related to the Fourier transform of the dipole (or dipole-derivative) correlation function. While the classical version of the approach (i.e., the classical correlation function) usually yields results close to normal-mode frequencies (in low temperature),[2–4] the quantum correlation function in principle leads to exact vibrational frequencies. There is then a great deal of effort focused on employing trajectory-based approximate quantum dynamics methods for vibrational spectroscopy of realistic molecular systems.[2,3,5–20] Such trajectory-based methods include the linearized semiclassical initial value representation (LSC-IVR)/ classical Wigner,[18,21–29] centroid molecular dynamics (CMD),[30–33] ring polymer molecular dynamics (RPMD),[34–39] and its thermostatted version (TRPMD).[3] These methods have become mature tools that enable the inclusion of quantum mechanics effects with (modified) MD trajectories in realistic systems. There are however some important situations in which some of these methods produce unphysical vibrational spectra (particularly for gas phase molecules). For instance, the "curvature problem" occurs in CMD,[3,4] while "artificial resonances" are inherent in RPMD.[3,4,9,15] Although the LSC-IVR and TRPMD do not suffer these intrinsic problems,

the full width at half maximum (FWHM) of the simulated peak is often too large for the vibrational spectrum of the gas phase molecule.[2,3] For example, they are not expected to distinguish the two stretching peaks of H_2O because the FWHM is typically ~200 cm^{-1} for the O–H stretch. It is then desirable for a trajectory-based approximate quantum approach to obtain a reasonably accurate peak position with a relatively small FWHM. Not less important, the simulated vibrational frequency (of the isolated molecule) should be insensitive to the change in temperature.

The purpose of this paper is to present a systematic investigation of path integral Liouville dynamics (PILD) for its applications to IR spectra of four realistic small but representative molecules, namely, OH, water, ammonia, and methane. Because both accurate PESs and exact vibrational frequencies are available for these systems, they offer benchmark tests for the methodology. Section II first gives the formulation for the dipole-derivative correlation function for the IR spectrum and then briefly reviews the PILD methodology for the quantum correlation function. Section III applies PILD to the IR spectra of the four benchmark molecular systems. The performance of PILD is investigated as a function of temperature and isotopic substitution. Conclusions and outlook follow in Section IV.

II. THEORY

A. Infrared spectrum and dipole-derivative correlation function

According to the Fermi golden rule of time-dependent perturbation theory in quantum mechanics, the experimental IR spectrum is directly related to the dipole-derivative absorption line shape[2,14,40] $I_{\dot{\mu}\dot{\mu}}^{kubo}(\omega)$ by

$$n(\omega)\,\alpha(\omega) = \frac{\beta\pi}{3cV\varepsilon_0} I_{\dot{\mu}\dot{\mu}}^{Kubo}(\omega),\qquad(1)$$

a)Electronic mail: jianliupku@pku.edu.cn

where the Beer-Lambert absorption constant $\alpha(\omega)$ and the refractive index $n(\omega)$ are two frequency-dependent properties, and $I_{\hat{\boldsymbol{\mu}}\hat{\boldsymbol{\mu}}}^{kubo}(\omega)$ is the Fourier transform of the (Kubo-transformed) collective dipole-derivative auto-correlation function,

$$I_{\hat{\boldsymbol{\mu}}\hat{\boldsymbol{\mu}}}^{Kubo}(\omega) = \frac{1}{2\pi} \int_{-\infty}^{\infty} dt \; e^{-i\omega t} \langle \hat{\boldsymbol{\mu}}(0)\hat{\boldsymbol{\mu}}(t) \rangle_{Kubo}. \quad (2)$$

Here, $\hat{\boldsymbol{\mu}}$ is the (collective) dipole-derivative operator (the change of the total dipole moment over time).

The quantum correlation function in Eq. (2) is of the general form

$$\langle \hat{A}(0)\hat{B}(t) \rangle = \frac{1}{Z} \text{Tr}\left(\hat{A}^{\beta} e^{i\hat{H}t/\hbar} \hat{B} e^{-i\hat{H}t/\hbar} \right), \quad (3)$$

where $\hat{A}_{Kubo}^{\beta} = \frac{1}{\beta} \int_0^{\beta} d\lambda e^{-(\beta-\lambda)\hat{H}} \hat{A} e^{-\lambda\hat{H}}$ for the Kubo-transformed version,[41] or $\hat{A}_{std}^{\beta} = e^{-\beta\hat{H}}\hat{A}$ for the standard version of the correlation function. Here, $Z = \text{Tr}\left[e^{-\beta\hat{H}} \right]$ ($\beta = 1/k_B T$) is the partition function, $\hat{H}$ the (time-independent) Hamiltonian of the system with the total number of degrees of freedom N, which we assume to be of standard Cartesian form

$$\hat{H} = \frac{1}{2}\hat{\mathbf{p}}^T \mathbf{M}^{-1}\hat{\mathbf{p}} + V(\hat{\mathbf{x}}), \quad (4)$$

where $\mathbf{M}$ is the diagonal "mass matrix" with elements $\{m_j\}$, and $\hat{\mathbf{p}}$ and $\hat{\mathbf{x}}$ are the momentum and coordinate operators, respectively, and $\hat{A}$ and $\hat{B}$ are operators relevant to the specific property of interest. For example, $\hat{A}^{\beta} = \hat{\boldsymbol{\mu}}_{Kubo}^{\beta} = \frac{1}{\beta} \int_0^{\beta} d\lambda e^{-(\beta-\lambda)\hat{H}} \hat{\boldsymbol{\mu}} e^{-\lambda\hat{H}}$ and $\hat{A} = \hat{B} = \hat{\boldsymbol{\mu}}$ for the Kubo-transformed collective dipole-derivative auto-correlation function $\langle \hat{\boldsymbol{\mu}}(0)\hat{\boldsymbol{\mu}}(t) \rangle_{Kubo}$.

B. Path integral Liouville dynamics

PILD is an imaginary time path integral based method for describing quantum dynamics effects.[42] It was derived from the phase space formulation of quantum mechanics.[43–46] PILD is able to combine the important properties of the LSC-IVR and of CMD/RPMD, which are as follows:

1. conserve the quantum canonical distribution for the thermal equilibrium system, and
2. treat both linear and nonlinear operators (i.e., linear or nonlinear functions of position or momentum operators) equally well and recover exact quantum correlation functions in the classical ($\hbar \to 0$), high-temperature ($\beta \to 0$), and harmonic limits.

1. Evaluation of the quantum correlation function

Evaluation of the quantum correlation function Eq. (3) with PILD takes the expression

$$\langle \hat{A}(0)\hat{B}(t) \rangle = \frac{1}{Z} \int d\mathbf{x}_0 \int d\mathbf{p}_0 \; \rho_W^{\text{eq}}(\mathbf{x}_0, \mathbf{p}_0)$$
$$\times f_{A\beta}^W(\mathbf{x}_0, \mathbf{p}_0) B_W(\mathbf{x}_t, \mathbf{p}_t), \quad (5)$$

where ρ_W^{eq}, B_W, and $f_{A\beta}^W$ are defined as

$$\rho_W^{\text{eq}}(\mathbf{x}, \mathbf{p}) = \frac{1}{(2\pi\hbar)^N} \int d\Delta\mathbf{x} \left\langle \mathbf{x} - \frac{\Delta\mathbf{x}}{2} \middle| e^{-\beta\hat{H}} \middle| \mathbf{x} + \frac{\Delta\mathbf{x}}{2} \right\rangle e^{i\Delta\mathbf{x}^T\mathbf{p}/\hbar},$$
$$(6)$$

$$B_W(\mathbf{x}, \mathbf{p}) = \int d\Delta\mathbf{x} \left\langle \mathbf{x} - \frac{\Delta\mathbf{x}}{2} \middle| \hat{B} \middle| \mathbf{x} + \frac{\Delta\mathbf{x}}{2} \right\rangle e^{i\Delta\mathbf{x}^T\mathbf{p}/\hbar}, \quad (7)$$

and

$$f_{A\beta}^W(\mathbf{x}, \mathbf{p}) = \frac{\int d\Delta\mathbf{x} \left\langle \mathbf{x} - \frac{\Delta\mathbf{x}}{2} \middle| \hat{A}^{\beta} \middle| \mathbf{x} + \frac{\Delta\mathbf{x}}{2} \right\rangle e^{i\Delta\mathbf{x}^T\mathbf{p}/\hbar}}{\int d\Delta\mathbf{x} \left\langle \mathbf{x} - \frac{\Delta\mathbf{x}}{2} \middle| e^{-\beta\hat{H}} \middle| \mathbf{x} + \frac{\Delta\mathbf{x}}{2} \right\rangle e^{i\Delta\mathbf{x}^T\mathbf{p}/\hbar}}, \quad (8)$$

respectively. It takes the same procedure to express the functions $f_{A\beta}^W$ and B_W as is often done in the Wigner phase space for the LSC-IVR.[2,25]

While expressing the Kubo-transformed collective dipole-derivative auto-correlation function $\langle \hat{\boldsymbol{\mu}}(0)\hat{\boldsymbol{\mu}}(t) \rangle_{Kubo}$ in Eq. (5) (as done in Ref. 2), one obtains

$$f_{A\beta}^W(\mathbf{x}_0, \mathbf{p}_0) B_W(\mathbf{x}_t, \mathbf{p}_t) \approx \left[\mathbf{p}_0^T \mathbf{M}_{therm}^{-1} \left(\frac{\partial\boldsymbol{\mu}}{\partial\mathbf{x}_0} \right) \right] \cdot \dot{\boldsymbol{\mu}}(\mathbf{x}_t, \mathbf{p}_t). \quad (9)$$

It is straightforward to derive Eq. (9) for Eq. (5) by virtue of the relation

$$\hat{\boldsymbol{\mu}}_{Kubo}^{\beta} = \frac{i}{\beta\hbar}\left[\hat{\boldsymbol{\mu}}, \; e^{-\beta\hat{H}} \right] \quad (10)$$

and the expansion of the total dipole moment (which can be a nonlinear function)

$$\boldsymbol{\mu}(\mathbf{x} + \Delta\mathbf{x}) = \boldsymbol{\mu}(\mathbf{x}) + \Delta\mathbf{x}^T \cdot \frac{\partial\boldsymbol{\mu}}{\partial\mathbf{x}}$$
$$+ \frac{1}{2}\Delta\mathbf{x}^T \cdot \frac{\partial^2\boldsymbol{\mu}}{\partial\mathbf{x}^2} \cdot \Delta\mathbf{x} + O(\Delta\mathbf{x}^3). \quad (11)$$

Here, the thermal mass matrix $\mathbf{M}_{therm}$ is defined by the quantum canonical distribution $\rho_W^{eq}(\mathbf{x},\mathbf{p})$, i.e.,

$$\frac{1}{Z}\rho_W^{eq}(\mathbf{x},\mathbf{p}) = \frac{1}{Z} \langle \mathbf{x}| e^{-\beta\hat{H}} |\mathbf{x}\rangle \left(\frac{\beta}{2\pi} \right)^{N/2} |\det(\mathbf{M}_{therm})|^{-1/2}$$
$$\times \exp\left[-\frac{\beta}{2}\mathbf{p}^T\mathbf{M}_{therm}^{-1}\mathbf{p} \right]. \quad (12)$$

Note that the thermal mass matrix $\mathbf{M}_{therm}$ is often different from the (diagonal) physical mass matrix $\mathbf{M}$ except in the high temperature or classical limit.[42] (Please see the Appendix for more discussion on the thermal mass matrix for the small molecule.)

The trajectory $(\mathbf{x}_t, \mathbf{p}_t)$ in Eq. (5) follows the equations of motion

$$\dot{\mathbf{x}}_t = \mathbf{M}^{-1}\mathbf{p}_t,$$
$$\dot{\mathbf{p}}_t = -\frac{\partial V_{eff}^{PILD}(\mathbf{x}_t, \mathbf{p}_t)}{\partial\mathbf{x}_t}, \quad (13)$$

with the effective force $-\frac{\partial V_{eff}^{PILD}(\mathbf{x},\mathbf{p})}{\partial\mathbf{x}}$ given by
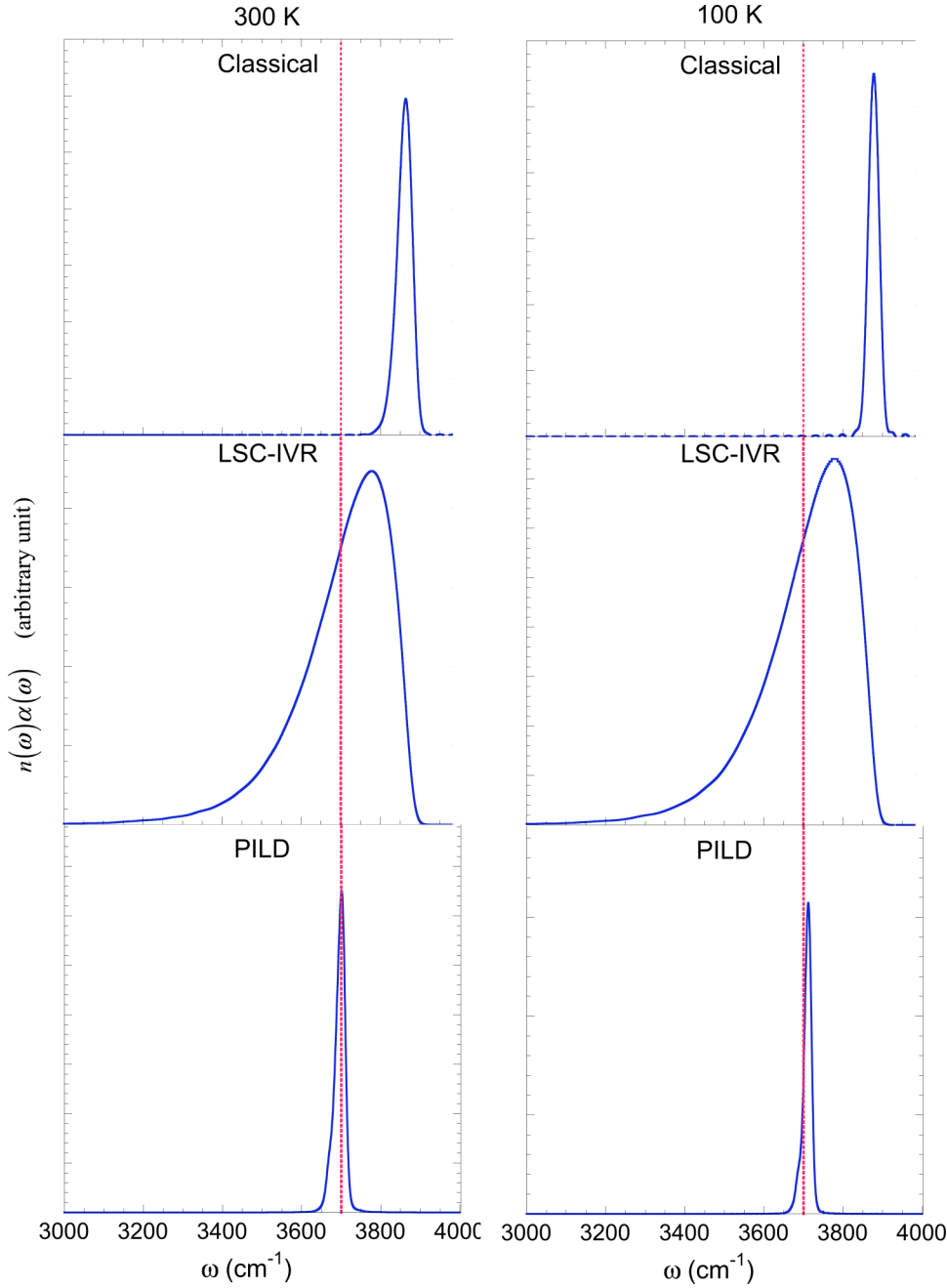
FIG. 1. The IR spectrum of the 3D Morse potential for the OH molecule. (The parameters of the potential are given in Ref. 2.) Dotted line represents the exact frequency.

$$-\frac{\partial}{\partial \mathbf{x}} V_{eff}^{PILD}(\mathbf{x},\mathbf{p}) = \frac{1}{\beta}\mathbf{M}_{therm}\mathbf{M}^{-1}\frac{\partial}{\partial \mathbf{x}}\ln\langle\mathbf{x}|e^{-\beta\hat{H}}|\mathbf{x}\rangle. \qquad (14)$$

Below, we show two important properties of the equations of motion Eq. (13).

Because of the quantum Liouville equation

$$\frac{\partial \hat{\rho}^{eq}}{\partial t} = -\frac{1}{i\hbar}\left[\hat{\rho}^{eq},\hat{H}\right], \qquad (15)$$

the quantum canonical distribution $\hat{\rho}^{eq} = e^{-\beta\hat{H}}$ is stationary. One can express Eq. (15) in the Wigner phase space[43–46] as

$$\frac{\partial \rho_W^{eq}(\mathbf{x},\mathbf{p};t)}{\partial t} = -\mathbf{p}^T\mathbf{M}^{-1}\frac{\partial \rho_W^{eq}}{\partial \mathbf{x}} + \left(\frac{\partial \rho_W^{eq}}{\partial \mathbf{p}}\right)^T \cdot \frac{\partial}{\partial \mathbf{x}}V_{eff}(\mathbf{x},\mathbf{p}). \qquad (16)$$

It is straightforward to verify that the right-hand side of Eq. (16) is equal to zero with Eqs. (12) and (14). That is, the equations of motion, Eq. (13), satisfy stationarity of the quantum canonical distribution

TABLE I. Peak positions of the O–H stretching mode at different temperatures. The parameters of the 3D Morse potential are given in Ref. 2.

	ω_{OH} (cm^{-1})		
T (K)	PILD	Exact	Harmonic approximation
1000	3700		
300	3700	3700.55	3886.56
100	3711		
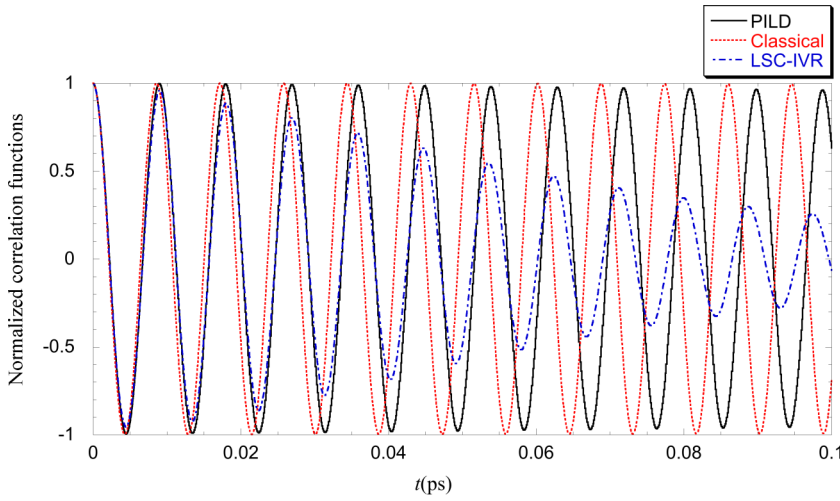
FIG. 2. Normalized dipole-derivative correlation functions $C_{\dot{\mu}\dot{\mu}}^{Kubo}(t)/$ $C_{\dot{\mu}\dot{\mu}}^{Kubo}(0)$ for the 3D Morse potential for $T = 100$ K.

function,

$$\frac{\partial \rho_W^{eq}(\mathbf{x},\mathbf{p};t)}{\partial t} = 0. \tag{17}$$

Note that the following equality always holds:

$$\frac{d\rho_W^{eq}(\mathbf{x}_t,\mathbf{p}_t;t)}{dt} = \frac{\partial \rho_W^{eq}(\mathbf{x}_t,\mathbf{p}_t;t)}{\partial t} + \left(\frac{\partial \rho_W^{eq}}{\partial \mathbf{x}_t}\right)^T \cdot \dot{\mathbf{x}}_t + \left(\frac{\partial \rho_W^{eq}}{\partial \mathbf{p}_t}\right)^T \cdot \dot{\mathbf{p}}_t. \tag{18}$$

Substituting Eqs. (13), (14), and (16) in Eq. (18), one obtains

$$\frac{d\rho_W^{eq}(\mathbf{x}_t,\mathbf{p}_t;t)}{dt} = 0. \tag{19}$$

Time-averaging Eq. (5) thus leads to

$$\begin{aligned}
\langle \hat{A}(0)\,\hat{B}(t) \rangle &= \frac{1}{T_0}\int_0^{T_0} dt' \langle A(t')\,B(t'+t) \rangle \\
&= \frac{1}{Z}\int d\mathbf{x}_0 \int d\mathbf{p}_0\, \rho_W^{eq}(\mathbf{x}_0,\mathbf{p}_0) \\
&\quad \times \frac{1}{T_0}\int_0^{T_0} dt'\, f_{A^\beta}^W(\mathbf{x}_{t'},\mathbf{p}_{t'})\, B_W(\mathbf{x}_{t+t'},\mathbf{p}_{t+t'}).
\end{aligned} \tag{20}$$

Eq. (20) offers a more economic way for evaluating the quantum correlation function than Eq. (5) does.

2. Path integral representation of the effective force

Inserting path integral beads to evaluate the term $\langle \mathbf{x} | e^{-\beta \hat{H}} | \mathbf{x} \rangle$ of Eq. (12) or Eq. (14) leads to

TABLE II. As in Table I, but for the 3D Morse potential with different parameters given in Ref. 3.

	ω_{OH} (cm^{-1})		
T (K)	PILD	Exact	Harmonic approximation
1000	3568		
300	3568	3568	3737.76
100	3578		

$$\langle \mathbf{x} | e^{-\beta \hat{H}} | \mathbf{x} \rangle \overset{\mathbf{x}_1 \equiv \mathbf{x}}{=} \lim_{P\to\infty} \int d\mathbf{x}_2 \cdots \int d\mathbf{x}_P \left(\frac{P}{2\pi\beta\hbar^2}\right)^{NP/2} |\mathbf{M}|^{P/2}$$

$$\times \exp\left\{ -\frac{P}{2\beta\hbar^2}\sum_{i=1}^{P}\left[(\mathbf{x}_{i+1}-\mathbf{x}_i)^T \mathbf{M}(\mathbf{x}_{i+1}-\mathbf{x}_i)\right] \right.$$

$$\left. -\frac{\beta}{P}\sum_{i=1}^{P} V(\mathbf{x}_i) \right\}, \tag{21}$$

where P is the number of path integral beads. Consider the staging transformation[47,48]

$$\begin{aligned}
\boldsymbol{\xi}_1 &= \mathbf{x}_1, \\
\boldsymbol{\xi}_j &= \mathbf{x}_j - \frac{(j-1)\mathbf{x}_{j+1}+\mathbf{x}_1}{j} \qquad \left(j=\overline{2,P}\right).
\end{aligned} \tag{22}$$

Its inverse transformation takes the following convenient recursive form:

$$\begin{aligned}
\mathbf{x}_1 &= \boldsymbol{\xi}_1, \\
\mathbf{x}_j &= \boldsymbol{\xi}_j + \frac{j-1}{j}\mathbf{x}_{j+1} + \frac{1}{j}\boldsymbol{\xi}_1 \qquad \left(j=\overline{2,P}\right).
\end{aligned} \tag{23}$$

Here, $\mathbf{x}_{P+1} \equiv \mathbf{x}_1$. If one defines

$$\phi(\boldsymbol{\xi}_1,\ldots,\boldsymbol{\xi}_P) = \frac{1}{P}\sum_{j=1}^{P} V(\mathbf{x}_j(\boldsymbol{\xi}_1,\ldots,\boldsymbol{\xi}_P)), \tag{24}$$

one then obtains the chain rule

$$\begin{aligned}
\frac{\partial \phi}{\partial \boldsymbol{\xi}_1} &= \sum_{i=1}^{P}\frac{\partial \phi}{\partial \mathbf{x}_i} = \frac{1}{P}\sum_{i=1}^{P} V'(\mathbf{x}_i), \\
\frac{\partial \phi}{\partial \boldsymbol{\xi}_j} &= \frac{\partial \phi}{\partial \mathbf{x}_j} + \frac{j-2}{j-1}\frac{\partial \phi}{\partial \boldsymbol{\xi}_{j-1}} \qquad \left(j=\overline{2,P}\right),
\end{aligned} \tag{25}$$

from Eqs. (22) and (23). If one chooses the corresponding fictitious masses $(\tilde{\mathbf{M}}_2,\ldots,\tilde{\mathbf{M}}_P)$ as

$$\tilde{\mathbf{M}}_j = \gamma_{ad}\frac{j}{j-1}\mathbf{M} \qquad \left(j=\overline{2,P}\right), \tag{26}$$

with $\gamma_{ad} \in (0,1]$ as an adiabatic parameter and also defines the adiabatic frequency ω_{ad} as

$$\omega_{ad} = \frac{1}{\beta\hbar}\sqrt{\frac{P}{\gamma_{ad}}}, \tag{27}$$

then the effective force of Eq. (14) can be obtained from

$$-\frac{1}{\beta}\frac{\partial}{\partial \mathbf{x}}\ln\langle\mathbf{x}|\,e^{-\beta\hat{H}}\,|\mathbf{x}\rangle \overset{\xi_1\equiv x_1\equiv x}{=} \frac{\lim\limits_{P\to\infty}\int d\xi_2\ldots\int d\xi_P\exp\left\{-\beta\left[\sum\limits_{j=2}^{P}\frac{1}{2}\omega_{ad}^2\xi_j^T\tilde{\mathbf{M}}_j\xi_j+\phi(\xi_1,\ldots,\xi_P)\right]\right\}\frac{1}{P}\sum\limits_{j=1}^{P}V'(\mathbf{x}_j)}{\lim\limits_{P\to\infty}\int d\xi_2\ldots\int d\xi_P\exp\left\{-\beta\left[\sum\limits_{j=2}^{P}\frac{1}{2}\omega_{ad}^2\xi_j^T\tilde{\mathbf{M}}_j\xi_j+\phi(\xi_1,\ldots,\xi_P)\right]\right\}}. \tag{28}$$

Taking advantage of the isomorphism strategy proposed by Chandler and Wolynes,[49] one can insert fictitious momenta $(\mathbf{p}_2,\ldots,\mathbf{p}_P)$ into Eq. (28), which leads to

$$-\frac{1}{\beta}\frac{\partial}{\partial \mathbf{x}}\ln\langle\mathbf{x}|\,e^{-\beta\hat{H}}\,|\mathbf{x}\rangle$$

$$\overset{\xi_1\equiv x_1\equiv x}{=} \frac{\lim\limits_{P\to\infty}\int\left(\prod\limits_{j=2}^{P}d\xi_j d\mathbf{p}_j\right)\exp\left\{-\beta\left[\sum\limits_{j=2}^{P}\left(\frac{1}{2}\mathbf{p}_j^T\tilde{\mathbf{M}}_j^{-1}\mathbf{p}_j+\frac{1}{2}\omega_{ad}^2\xi_j^T\tilde{\mathbf{M}}_j\xi_j\right)+\phi(\xi_1,\ldots,\xi_P)\right]\right\}\frac{1}{P}\sum\limits_{j=1}^{P}V'(\mathbf{x}_j)}{\lim\limits_{P\to\infty}\int\left(\prod\limits_{j=2}^{P}d\xi_j d\mathbf{p}_j\right)\exp\left\{-\beta\left[\sum\limits_{j=2}^{P}\left(\frac{1}{2}\mathbf{p}_j^T\tilde{\mathbf{M}}_j^{-1}\mathbf{p}_j+\frac{1}{2}\omega_{ad}^2\xi_j^T\tilde{\mathbf{M}}_j\xi_j\right)+\phi(\xi_1,\ldots,\xi_P)\right]\right\}}. \tag{29}$$
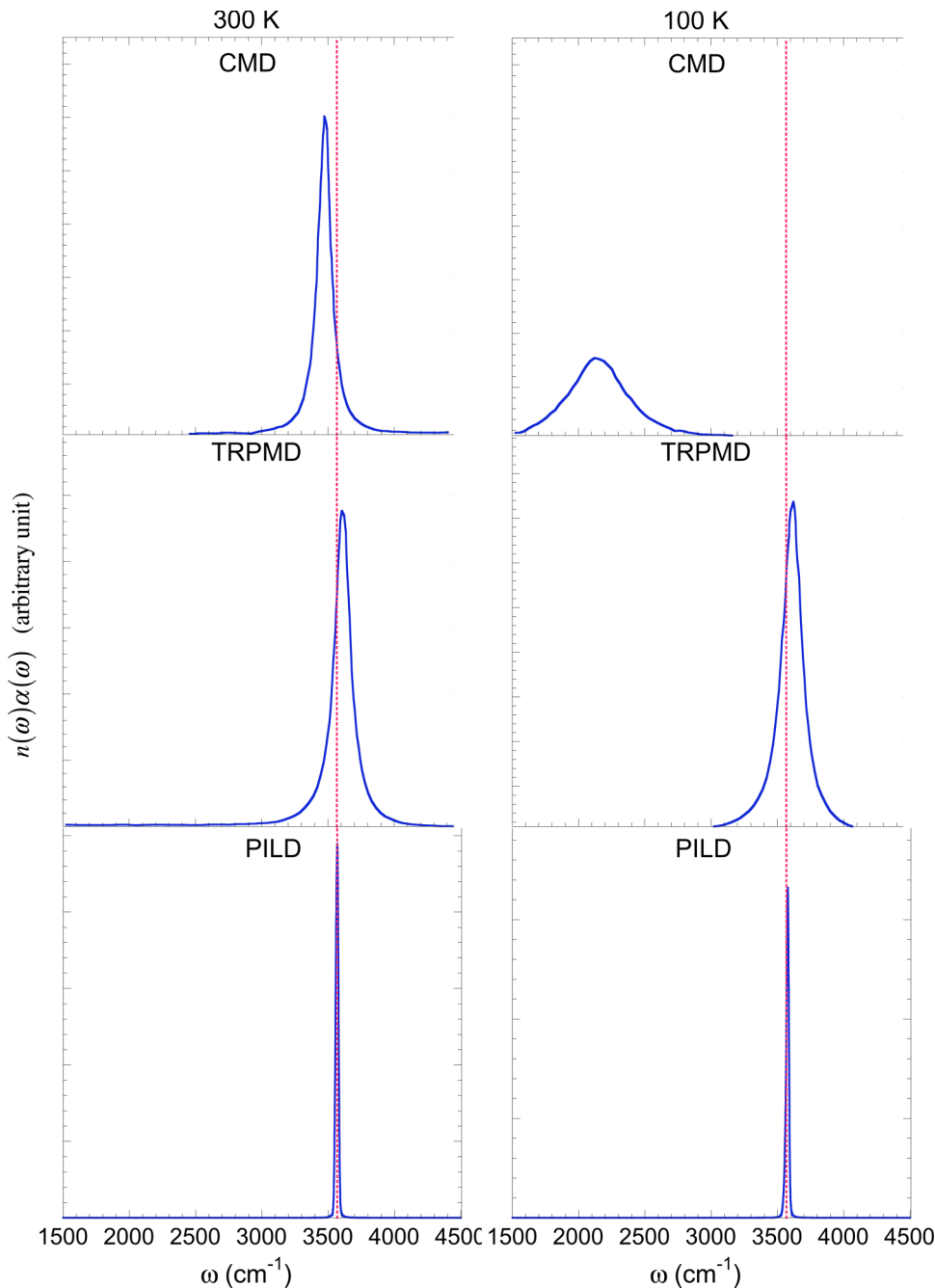

FIG. 3. As in Fig. 1, but for the 3D Morse model with different parameters as given in Ref. 3. (Both CMD and TRPMD results are from Ref. 3.)
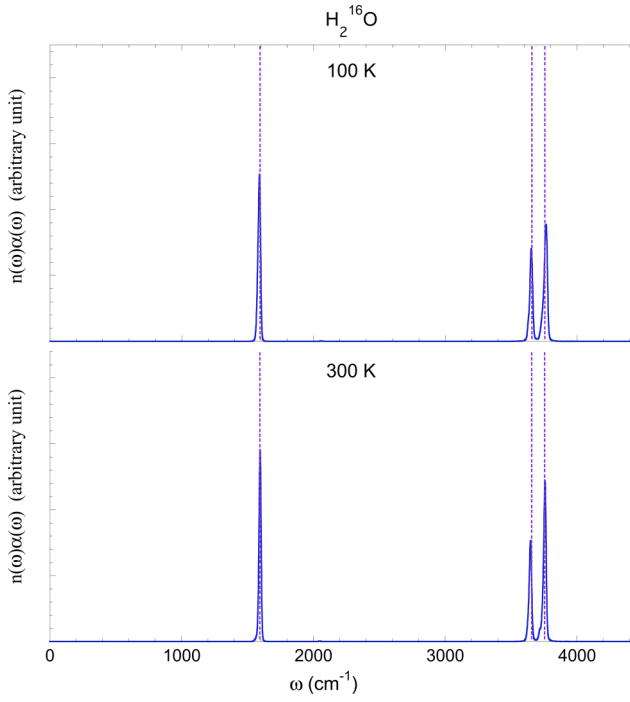
FIG. 4. The IR spectrum for $H_2^{16}O$ for both 300 K and 100 K. Purple dotted lines represent exact frequencies.

TABLE III. Peak positions of the $H_2^{16}O$ molecule at different temperatures. PES and exact results from Ref. 56 (unit: cm^{-1}).

PILD			
100 K	300 K	Exact	Harmonic approximation
1590	1596	1594.78	1652.2
3655	3648	3657.04	3821.62
3764	3758	3755.96	3932.21

$(\boldsymbol{\xi}_2, \ldots, \boldsymbol{\xi}_P, \mathbf{p}_2, \ldots, \mathbf{p}_P)$ in PILD, Eq. (30) becomes

$$\dot{\boldsymbol{\xi}}_1 \equiv \dot{\mathbf{x}}_1 \equiv \dot{\mathbf{x}} = \mathbf{M}^{-1}\mathbf{p},$$

$$\dot{\mathbf{p}}_1 \equiv \dot{\mathbf{p}} = -\mathbf{M}_{therm}\mathbf{M}^{-1}\frac{\partial \phi}{\partial \boldsymbol{\xi}_1} = -\mathbf{M}_{therm}\mathbf{M}^{-1}\left(\frac{1}{P}\sum_{j=1}^{P}\frac{\partial V(\mathbf{x}_j)}{\partial \mathbf{x}_j}\right),$$

$$\dot{\boldsymbol{\xi}}_j = \tilde{\mathbf{M}}_j^{-1}\mathbf{p}_j, \tag{31}$$

$$\dot{\mathbf{p}}_j = -\omega_{ad}^2\tilde{\mathbf{M}}_j\boldsymbol{\xi}_j - \frac{\partial \phi}{\partial \boldsymbol{\xi}_j} - \gamma_{Lang}\mathbf{p}_j$$

$$+ \sqrt{\frac{2\gamma_{Lang}}{\beta}}\left(\tilde{\mathbf{M}}_j\right)^{1/2}\boldsymbol{\eta}_j(t) \qquad \left(j = \overline{2,P}\right).$$

Here, $\boldsymbol{\eta}_j(t)$ is a vector. Its element $\eta_j^i(t)$ is an independent Gaussian-distributed random number with zero mean and unit variance [$\langle \eta_j^i(t) \rangle = 0$ and $\langle \eta_j^i(t)\eta_j^i(t') \rangle = \delta(t - t')$], which is different for each physical degree of freedom $\left(i = \overline{1,N}\right)$, each staging mode $\left(j = \overline{2,P}\right)$, and each time step. The Langevin friction coefficient γ_{Lang} is the same for all staging modes $\left(j = \overline{2,P}\right)$ and all degrees of freedom $\left(i = \overline{1,N}\right)$ because they share the same frequency ω_{ad}. It has been demonstrated that the PILD result is insensitive to the choice of the friction coefficient γ_{Lang} around the optimum value

$$\gamma_{Lang}^{opt} = \omega_{ad} \tag{32}$$

that is expected to offer the most efficient sampling in the free particle limit for the variables $(\boldsymbol{\xi}_2, \ldots, \boldsymbol{\xi}_P)$ and then for the estimator $\frac{1}{P}\sum_{j=1}^{P}V'(\mathbf{x}_j)$ in Eq. (29) for evaluating the effective force.[42,52]

Besides the velocity Verlet algorithm[50,51] for PILD proposed in Ref. 42, a more efficient algorithm for PILD[52,53] has recently been developed from the BAOAB integrator.[54,55] Such a BAOAB algorithm for propagating the PILD trajectory through a time interval Δt is[52,53]

$$\mathbf{p}_1 \leftarrow \mathbf{p}_1 - \mathbf{M}_{therm}\mathbf{M}^{-1}\frac{\partial \phi}{\partial \boldsymbol{\xi}_1}\frac{\Delta t}{2},$$

$$\mathbf{p}_j \leftarrow \mathbf{p}_j - \frac{\partial \phi}{\partial \boldsymbol{\xi}_j}\frac{\Delta t}{2} \qquad \left(j = \overline{2,P}\right), \tag{33}$$

The effective force of Eq. (14) can then be obtained by sampling $(\boldsymbol{\xi}_2, \ldots, \boldsymbol{\xi}_P, \mathbf{p}_2, \ldots, \mathbf{p}_P)$ in a molecular dynamics (MD) scheme. Note that all the staging variables $(\boldsymbol{\xi}_2, \ldots, \boldsymbol{\xi}_P)$ share the same time scale that can be *well separated* from the time scale of $\boldsymbol{\xi}_1 \equiv \mathbf{x}$ with the choice of the adiabatic parameter γ_{ad}. When the separation of time scales holds, Eqs. (13), (14), and (29) lead to

$$\dot{\boldsymbol{\xi}}_1 \equiv \dot{\mathbf{x}}_1 \equiv \dot{\mathbf{x}} = \mathbf{M}^{-1}\mathbf{p},$$

$$\dot{\mathbf{p}}_1 \equiv \dot{\mathbf{p}} = -\mathbf{M}_{therm}\mathbf{M}^{-1}\frac{\partial \phi}{\partial \boldsymbol{\xi}_1} = -\mathbf{M}_{therm}\mathbf{M}^{-1}\left(\frac{1}{P}\sum_{j=1}^{P}\frac{\partial V(\mathbf{x}_j)}{\partial \mathbf{x}_j}\right),$$

$$\dot{\boldsymbol{\xi}}_j = \tilde{\mathbf{M}}_j^{-1}\mathbf{p}_j, \tag{30}$$

$$\dot{\mathbf{p}}_j = -\omega_{ad}^2\tilde{\mathbf{M}}_j\boldsymbol{\xi}_j - \frac{\partial \phi}{\partial \boldsymbol{\xi}_j} \qquad \left(j = \overline{2,P}\right).$$

The equations of motion for $(\boldsymbol{\xi}_2, \ldots, \boldsymbol{\xi}_P, \mathbf{p}_2, \ldots, \mathbf{p}_P)$ in Eq. (30) must be coupled to a thermostatting method to ensure a proper canonical distribution for $(\boldsymbol{\xi}_2, \ldots, \boldsymbol{\xi}_P, \mathbf{p}_2, \ldots, \mathbf{p}_P)$, while the quantum phase space variables $(\boldsymbol{\xi}_1, \mathbf{p}_1) \equiv (\mathbf{x}, \mathbf{p})$ should *not* be thermostatted. When the adiabatic parameter $\gamma_{ad} \to 0$, Eq. (30) approaches the full adiabatic version of PILD.

3. Algorithm for PILD with Langevin thermostat

When a simple (white noise) Langevin dynamics[50,51] is employed to thermostat the staging path integral variables

$$\boldsymbol{\xi}_1 \leftarrow \boldsymbol{\xi}_1 + \mathbf{M}^{-1}\mathbf{p}_1\frac{\Delta t}{2},$$

$$\begin{pmatrix} \boldsymbol{\xi}_j \\ \mathbf{p}_j \end{pmatrix} \leftarrow \begin{pmatrix} \cos(\omega_{ad}\Delta t/2)\,\mathbf{1} & \sin(\omega_{ad}\Delta t/2)/\omega_{ad}\,\tilde{\mathbf{M}}_j^{-1} \\ -\omega_{ad}\sin(\omega_{ad}\Delta t/2)\,\tilde{\mathbf{M}}_j & \cos(\omega_{ad}\Delta t/2)\,\mathbf{1} \end{pmatrix}\begin{pmatrix} \boldsymbol{\xi}_j \\ \mathbf{p}_j \end{pmatrix} \qquad \left(j = \overline{2,P}\right), \tag{34}$$

$$\mathbf{p}_j \leftarrow c_1 \mathbf{p}_j + c_2 \sqrt{\frac{1}{\beta}} (\tilde{\mathbf{M}}_j)^{1/2} \boldsymbol{\eta}_j \qquad \left(j = \overline{2,P} \right), \qquad (35)$$

$$\boldsymbol{\xi}_1 \leftarrow \boldsymbol{\xi}_1 + \mathbf{M}^{-1} \mathbf{p}_1 \frac{\Delta t}{2},$$

$$\begin{pmatrix} \boldsymbol{\xi}_j \\ \mathbf{p}_j \end{pmatrix} \leftarrow \begin{pmatrix} \cos(\omega_{ad}\Delta t/2)\, \mathbf{1} & \sin(\omega_{ad}\Delta t/2)/\omega_{ad}\, \tilde{\mathbf{M}}_j^{-1} \\ -\omega_{ad}\sin(\omega_{ad}\Delta t/2)\, \tilde{\mathbf{M}}_j & \cos(\omega_{ad}\Delta t/2)\, \mathbf{1} \end{pmatrix} \begin{pmatrix} \boldsymbol{\xi}_j \\ \mathbf{p}_j \end{pmatrix} \qquad \left(j = \overline{2,P} \right), \qquad (36)$$

$$\mathbf{p}_1 \leftarrow \mathbf{p}_1 - \mathbf{M}_{therm}\mathbf{M}^{-1} \frac{\partial \phi}{\partial \boldsymbol{\xi}_1} \frac{\Delta t}{2},$$
$$\mathbf{p}_j \leftarrow \mathbf{p}_j - \frac{\partial \phi}{\partial \boldsymbol{\xi}_j} \frac{\Delta t}{2} \qquad \left(j = \overline{2,P} \right). \qquad (37)$$

Here, $\boldsymbol{\eta}_j$ is the independent Gaussian-distributed random number vector as discussed for Eq. (31), which is different for each invocation of Eq. (35), and the coefficients c_1 and c_2 are

$$c_1 = \exp\left[-\gamma_{Lang}\Delta t \right],$$
$$c_2 = \sqrt{1 - (c_1)^2}. \qquad (38)$$

While the forces in Eq. (33) are obtained from the previous time step, those in Eq. (37) at the current time step can be efficiently evaluated by chain rule Eq. (25).

III. RESULTS AND DISCUSSIONS

PILD approaches the LSC-IVR/classical Wigner and then produces exact correlation functions in the harmonic limit.[42] So we focus on testing PILD for anharmonic systems in the paper. Below we apply PILD to a 3D shifted Morse model for an OH molecule[2,3] and then to accurate PESs for H$_2$O, NH$_3$, CH$_4$, and their isotope molecules where exact quantum vibrational frequencies are available.[56–58] Path integral molecular dynamics (PIMD) is used for equilibrating the molecular system and for evaluating the average thermal mass matrix $\mathbf{M}_{therm}$ before PILD is employed for real time dynamics. The dipole moment $\boldsymbol{\mu}$ and its time derivative $\dot{\boldsymbol{\mu}}$ are obtained by the point charge model.

A. Simulation details

We first consider a 3D shifted Morse potential for the 2-atom molecule OH,

$$V(r) = D_e \left(1 - \exp\left[-\alpha(|\mathbf{r}| - r_{eq})^2 \right] \right). \qquad (39)$$

Liu *et al.* have applied the LSC-IVR to this model (with the parameters listed in Ref. 2). More recently, Rossi *et al.* have used the same model with slightly different parameters for testing CMD, RPMD, and TRPMD.[3] Both sets of parameters with the model are used to test the accuracy of the PILD vibrational spectrum. $P = 640$ path integral beads are used in PIMD and PILD for $T = 100$ K, while $P = 256$ for $T = 300$ K and $P = 64$ for $T = 1000$ K. Converged PILD results are obtained with the adiabatic parameter $\gamma_{ad} = 10^{-4}$. While the

time interval for PIMD is ~0.006 fs, that for PILD is decreased to ~0.0012 fs in order to achieve ~1 cm^{-1} accuracy for the peak position of the spectrum. The quantum correction factors are evaluated every 100 steps in the PIMD trajectory. 32 PIMD trajectories with each propagated up to ~120 ps are used for obtaining the average thermal mass matrix. Each PILD trajectory is propagated up to ~5 ps and 120 such trajectories (from different initial conditions) are collected for evaluating the dipole-derivative correlation function with time averaging [Eq. (20)].

We then apply PILD to simulate H$_2$^{16}O and its various isotope molecules with the accurate PES developed by Partridge and Schwenke from extensive *ab initio* calculations and experimental data.[56] As the explicit form of the PES is available, that of the force and that of the Hessian of the PES can be expressed. The parameters for PIMD and PILD simulations are the same as those for the Morse model for OH. Each PILD trajectory is propagated up to 36 ps and 32 such trajectories (from different initial conditions) are collected for obtained dipole-derivative correlation function. The IR spectrum of H$_2$^{16}O is simulated for both $T = 300$ K and $T = 100$ K to test temperature effects. We then study the isotope molecules (H$_2$^{17}O, H$_2$^{18}O, HD^{16}O, HT^{16}O, D$_2$^{16}O, D$_2$^{18}O, and T$_2$^{16}O) for $T = 300$ K. Exact quantum results of these systems are available in Ref. 56 for comparison.

The third system is NH$_3$. Its accurate PES was recently developed by Yurchenko *et al.*[57] Since tunneling splitting effects are involved in its vibrational spectrum, the system presents a challenging test for the method. The explicit form of the force and that of the Hessian are obtained for the PES. The parameters used for converged results for the system are the same as those for the water molecule. PILD results are obtained for both $T = 300$ K and $T = 100$ K for comparison. Because exact quantum results are not available for its isotope molecules for the PES,[57] we only focus on the simulation of NH$_3$.

The last systems are CH$_4$ and its isotope molecules. Wang and Carrington, Jr. have recently used experimental data and a contracted basis Lanczos method to determine an accurate methane PES.[58] We explicitly express the force and the Hessian of the PES for computation. Simulations of the systems employ the same parameters as those for the water molecule. We first study the spectrum of ^{12}CH$_4$ at $T = 300$ K and that at $T = 100$ K. ^{13}CH$_4$, ^{12}CH$_3$D, and ^{12}CHD$_3$ are then simulated for $T = 300$ K for studying isotope effects in the spectrum.

B. Results and discussions

1. 3D Morse model for OH

It has been shown in Ref. 2 that both the LSC-IVR and MD are able to obtain the correct vibrational frequency for a shifted 3D harmonic model for an isolated OH molecule. When a 3D Morse model is employed for the O–H stretch,

the LSC-IVR greatly improves over MD for the peak position in the IR spectrum, but the unphysical decay of the LSC-IVR correlation function leads to the over-broadening of the spectrum.[2] For example, the FWHM is around 200 cm^{-1} at 100 K.

Fig. 1 depicts comparison of the exact vibrational frequency to the spectra obtained from MD, the LSC-IVR,
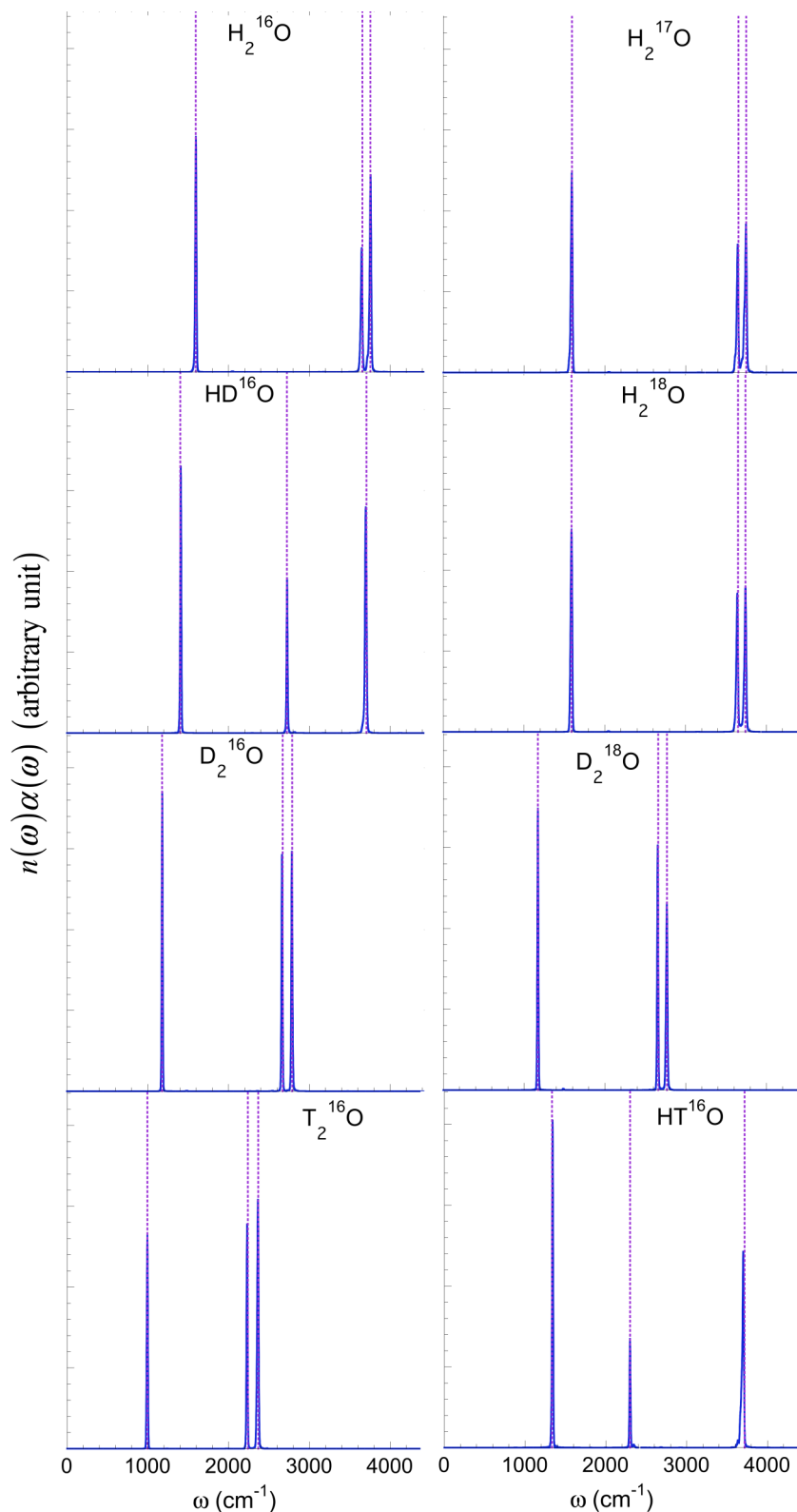
FIG. 5. IR spectra for various isotope water molecules for 300 K. Purple dotted lines represent exact frequencies.

and PILD for the 3D Morse potential (with the parameters in Ref. 2). The FWHM of the PILD peak is about 10–15 cm^{-1}, which is significantly smaller than that of the LSC-IVR result. The peak position of the PILD spectrum is relatively insensitive to the temperature as shown in Table I. While the PILD result for 300 K or higher temperature is nearly identical to the exact vibrational frequency, that for low temperature (100 K) is slightly shifted by ~10 cm^{-1}. Fig. 2 then compares the normalized dipole-derivative correlation functions. While PILD and the LSC-IVR results are in good agreement in short time, PILD is able to improve over the LSC-IVR for long time behaviors, leading to a small FWHM of the peak. As discussed before,[42,45,46] this is because that PILD conserves the mapping quantum canonical distribution even for anharmonic systems.

Witt *et al.* have shown that the "curvature problem" of CMD and "artificial resonances" of RPMD exist even for a shifted 3D harmonic model.[4] Rossi *et al.* have further demonstrated that such problems still exist for a more realistic model—the 3D Morse potential (with the parameter in Ref. 3). We apply PILD to the same model and collect the results at different temperatures in Table II. Fig. 3 illustrates comparison of the PILD spectrum to the CMD and TRPMD spectra reported in Ref. 3. [Fig. 4 of Ref. 3 can be compared with Fig. 3 of this article.] As suggested by the results on the peak position and on the FWHM for either $T = 300$ K or $T = 100$ K, PILD does not suffer from the "curvature problem," "artificial resonances," and over-broadening of the spectrum as inherent in other imaginary time path integral based methods.

2. Water

The difference between the frequencies of the symmetric and asymmetric stretching modes of the water molecule ($H_2^{16}O$) in gas phase is about 100 cm^{-1}. The two distinct stretching peaks are expected to merge into a broad one when the FWHM produced by a method is more than ~100 cm^{-1}. Fig. 4 demonstrates the PILD spectrum for 300 K and that for 100 K. Because the FWHM of the PILD peak is small, it leads to two well-separated stretching peaks for both temperatures. The peak positions shown in Fig. 4 and listed in Table III suggest that PILD dramatically improves over the harmonic approximation. The PILD peaks are relatively insensitive to temperature—no more than 7 cm^{-1} difference between the results for 300 K and for 100 K. This agrees well with the fact that exact vibrational frequencies of the isolated small molecule are independent of temperature.

Fig. 5 and Table IV then present the spectra and peak positions of the various isotope molecules ($H_2^{17}O$, $H_2^{18}O$, $HD^{16}O$, $HT^{16}O$, $D_2^{16}O$, $D_2^{18}O$, and $T_2^{16}O$) for 300 K. All peaks are sharp and their positions are in good agreement with exact vibrational frequencies (the difference is no more than 10 cm^{-1}). Comparison of the peaks of $H_2^{16}O$, $D_2^{16}O$, and $T_2^{16}O$ to the exact results suggests that PILD robustly captures isotope effects for the system. This is supported by comparing the peaks of $H_2^{16}O$, $H_2^{17}O$, and $H_2^{18}O$, those of $HD^{16}O$ and $HT^{16}O$, and those of $D_2^{16}O$ and $D_2^{18}O$.

TABLE IV. Peak positions of isotope molecules of H_2O at 300 K. PES and exact results from Ref. 56 (unit: cm^{-1}).

	PILD	Exact	Harmonic approximation
$H_2^{17}O$	1590	1591.33	1648.59
	3644	3653.14	3817.37
	3746	3748.32	3923.77
$H_2^{18}O$	1588	1588.3	1645.35
	3641	3649.68	3813.59
	3742	3741.57	3916.25
$HD^{16}O$	1409	1403	1448.58
	2725	2724	2815.86
	3699	3707.5	3879.13
$HT^{16}O$	1340	1332	1374.09
	2298	2299.8	2362.1
	3700	3716.6	3878
$D_2^{16}O$	1179	1178	1209.27
	2662	2671	2754.78
	2784	2788	2881.05
$D_2^{18}O$	1171	1170	1200.69
	2654	2660	2743.28
	2767	2767	2859.23
$T_2^{16}O$	994	995	1017.33
	2228	2237	2293.5
	2362	2366	2432.62

3. Ammonia

NH_3 presents a benchmark system for testing dynamics methods. Of the six vibrational modes of the molecule, two are degenerate around 1627 cm^{-1} and two more around 3444 cm^{-1}.
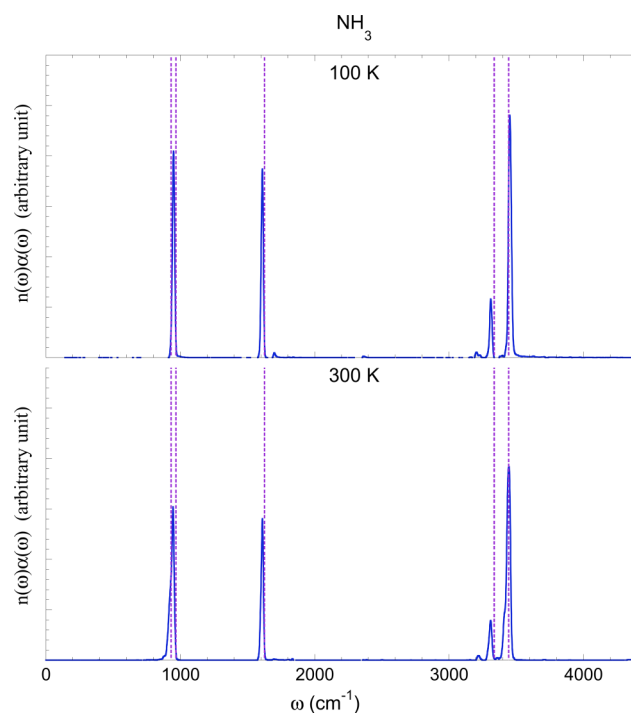

FIG. 6. The IR spectrum for NH_3 for both 300 K and 100 K. Purple dotted lines represent exact frequencies.

TABLE V. Peak positions of the NH$_3$ molecule at different temperatures. PES and exact results from Ref. 57 (unit: cm^{-1}).

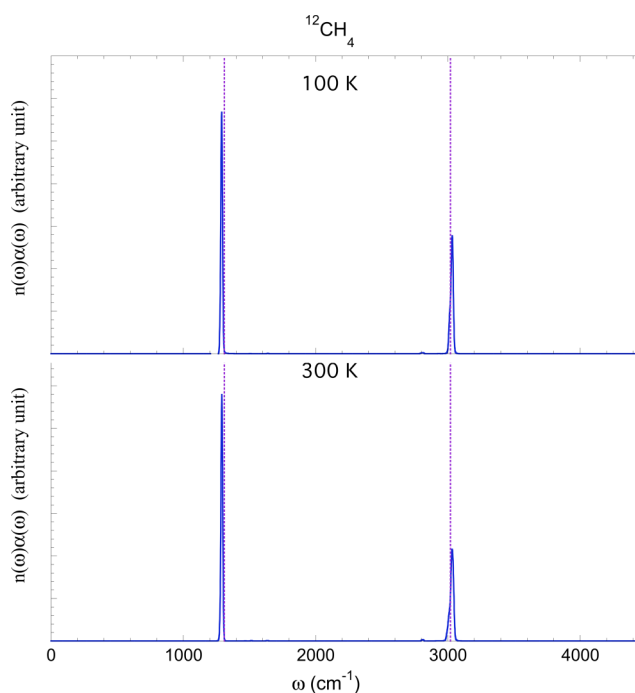| PILD		Exact	
100 K	300 K	(with tunneling splitting)	Harmonic approximation
950	946	968.12/932.50	1051.74
1610	1611	1626.3/1627.4	1667.21
3311	3310	3336.09/3337.14	3487.34
3453	3446	3443.72/3444.06	3640.62

TABLE VI. Peak positions of the ^{12}CH$_4$ molecule at different temperatures. PES and exact results from Ref. 58 (unit: cm^{-1}).

PILD		Exact	Harmonic approximation
100 K	300 K		
1288	1292	1310.47	1343.12
3030	3033	3019.43	3160.68

and three such ones about 3019 cm^{-1}. As demonstrated in Fig. 7 and Table VI, comparison of the exact vibrational frequencies to the PILD results for both 300 K and 100 K suggests that the PILD peaks are relatively stable against the

The tunneling splitting in the lowest frequency is ∼35 cm^{-1}, that in the highest frequency is ∼0.3 cm^{-1}, and those in the other two frequencies are about 1 cm^{-1}.

Fig. 6 and Table V show the spectra and peak positions for 300 K and 100 K. The difference between the PILD peak position and the exact result is less than ∼17 cm^{-1}. Any PILD peak position for 100 K is no more than 7 cm^{-1} different from that for 300 K, which demonstrates that PILD is reasonably stable when the temperature of the system changes. As discussed in the literature,[42,43,45,46] PILD is not able to describe true quantum coherence/interference in the correlation function. The tunneling splitting is then beyond the limit of the PILD approach. Although the FWHM of the PILD peak is no more than 15 cm^{-1}, PILD fails to capture the tunneling splitting even for the lowest vibrational frequency (that is ∼35 cm^{-1}).

4. Methane

^{12}CH$_4$ has nine vibrational modes but only four fundamental frequencies due to symmetry. Only six modes are IR active—three degenerate modes around 1310 cm^{-1}

FIG. 7. The IR spectrum for ^{12}CH$_4$ for both 300 K and 100 K. Purple dotted lines represent exact frequencies.
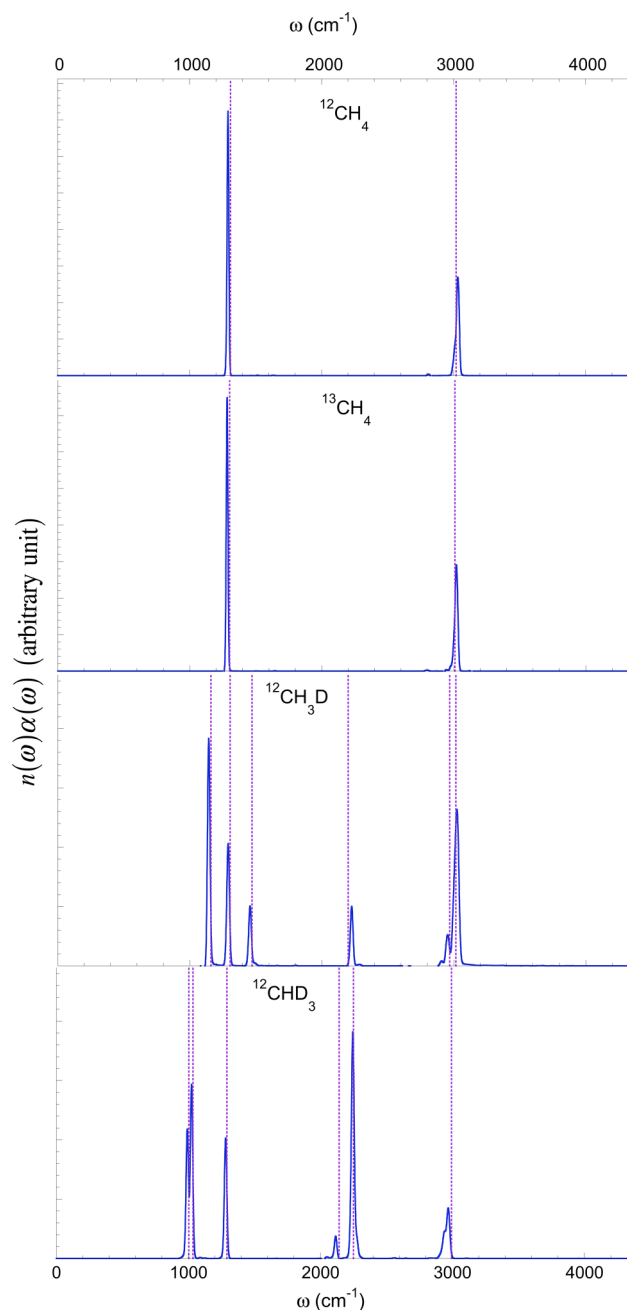

FIG. 8. IR spectra for isotope methane molecules for 300 K. Purple dotted lines represent exact frequencies.

TABLE VII. Peak positions of isotope molecules of CH_4 at 300 K. PES and exact results from Ref. 58 (unit: cm^{-1}).

	PILD	Exact	Harmonic approximation
$^{13}CH_4$	1283	1302.5	1334.78
	3020	3009.47	3149.43
$^{12}CH_3D$	1144	1160.74	1186.56
	1292	1306.40	1337.55
	1457	1472.13	1509.08
	2227	2199.86	2287.63
	2949	2969.75	3074.09
	3026	3016.65	3160.42
$^{12}CHD_3$	992	1004	1023.67
	1025	1035.5	1054.63
	1283	1292.42	1321.60
	2116	2142.78	2193.17
	2246	2250.66	2339.87
	2971	2992.88	3133.85

change in temperature. Its isotope molecule $^{13}CH_4$ shares the same symmetry. PILD is able to capture the changes in the IR spectrum due to isotopic substitution.

Either $^{12}CH_3D$ or $^{12}CHD_3$ breaks the symmetry of CH_4. All nine vibrational modes are then IR active, leading to six fundamental frequencies in the IR spectrum. As shown in Fig. 8 and Table VII, PILD faithfully produces six distinct peaks in the IR spectrum of either molecules. Even when the difference between the exact two lowest vibrational frequencies of $^{12}CHD_3$ is only about 32 cm^{-1}, the two corresponding PILD peaks are soundly separated because the FWHM of each PILD peak is small enough. All peak positions agree reasonably well with exact results—the deviation is no larger than 28 cm^{-1}.

IV. CONCLUDING REMARKS

Developed from the phase space formulation of quantum mechanics,[42–46] PILD offers an accessible method (in the Wigner phase space) to improve over the LSC-IVR on the long-time dynamical behaviors. Its applications to H_2O, NH_3, CH_4, and their various isotope molecules demonstrate that PILD is a potentially useful trajectory-based approximate quantum dynamics approach for simulating vibrational spectra of small molecular systems. The PILD peak position is relatively insensitive to the change in temperature. Its deviation from the exact result is no more than 30 cm^{-1} for all the benchmark tests in the article. PILD produces a small FWHM (less than ~15 cm^{-1}) and is then able to distinct two peaks even when the difference of their positions is ~30 cm^{-1}. Because PILD is not able to describe true quantum coherence/interference effects,[42] it fails to capture such as the tunneling splitting in the spectrum (as shown in Fig. 6). It will be interesting in future work to test PILD for larger realistic molecular systems and to see how PILD complements the LSC-IVR/classical Wigner and other successful trajectory-based approximate quantum dynamics methods for condensed phase systems.[3,18,21–27,29–39,59–62]

APPENDIX: EVALUATION OF THE THERMAL MASS MATRIX

As in the standard normal-mode analysis, mass-weighted Hessian matrix elements are given by

$$H_{kl} = \frac{1}{\sqrt{m_k m_l}} \frac{\partial^2 V}{\partial x_k \partial x_l}, \tag{A1}$$

where m_k represents the mass of the kth degree of freedom with N the total number of degrees of freedom. The Hamiltonian around $\mathbf{x}$ can be expanded to 2nd order as

$$H(\mathbf{x} + \Delta\mathbf{x}) \approx \frac{1}{2}\mathbf{p}^T\mathbf{M}^{-1}\mathbf{p} + V(\mathbf{x}) + \left(\frac{\partial V}{\partial \mathbf{x}}\right)^T \Delta\mathbf{x} + \frac{1}{2}\Delta\mathbf{x}^T H \Delta\mathbf{x}. \tag{A2}$$

The eigenvalues of the mass-weighted Hessian matrix produce normal-mode frequencies $\{\omega_k\}$, i.e.,

$$\mathbf{T}^T H \mathbf{T} = \lambda, \tag{A3}$$

with λ a diagonal matrix with the elements $\{(\omega_k)^2\}$ and $\mathbf{T}$ an orthogonal matrix. If $\mathbf{b}_k$ is the kth column of the matrix $\mathbf{T}$, then

$$H\mathbf{b}_k = \mathbf{b}_k \lambda_k. \tag{A4}$$

The mass-weighted normal mode coordinates $\mathbf{X}$ are given in terms of the Cartesian variables $\mathbf{x}$ by

$$\mathbf{X} = \mathbf{T}^T \mathbf{M}^{1/2}\mathbf{x}. \tag{A5}$$

In terms of the phase space variables $(\mathbf{x}, \mathbf{p})$, the density distribution function becomes

$$\rho_W^{eq}(\mathbf{x}, \mathbf{p}) = \langle \mathbf{x}| e^{-\beta \hat{H}} |\mathbf{x}\rangle \left(\frac{\beta}{2\pi}\right)^{N/2} \left|\det\left(\mathbf{M}_{therm}^{-1}\right)\right|^{1/2}$$

$$\times \exp\left[-\frac{\beta}{2}\mathbf{p}^T\mathbf{M}_{therm}^{-1}\mathbf{p}\right], \tag{A6}$$

with the thermal mass matrix $\mathbf{M}_{therm}$ given by

$$\mathbf{M}_{therm}^{-1}(\mathbf{x}) = \mathbf{M}^{-1/2}\mathbf{T}\mathbf{Q}(\mathbf{x})^{-1}\mathbf{T}^T\mathbf{M}^{-1/2} \tag{A7}$$

or

$$\mathbf{M}_{therm}(\mathbf{x}) = \mathbf{M}^{1/2}\mathbf{T}\mathbf{Q}(\mathbf{x})\mathbf{T}^T\mathbf{M}^{1/2} \tag{A8}$$

and with the diagonal matrix $\mathbf{Q} = \{Q(u_k)\}$. The quantum correction factor $Q(u)$ with the local Gaussian approximation (LGA) ansatz[25] for both real and imaginary frequencies is given by

$$Q(u) = \begin{cases} \dfrac{u/2}{\tanh(u/2)} & \text{for real } u = \beta\hbar\omega \\ = \dfrac{1}{Q(u_i)} = \dfrac{\tanh(u_i/2)}{u_i/2} & \text{for imaginary } u \ (u = iu_i) \end{cases}. \tag{A9}$$

Consider the equilibrium configuration $\mathbf{x}_0$ of the molecule (i.e., the global minimum of the PES). $\mathbf{b}_{0k}$ is the kth column of the orthogonal matrix $\mathbf{T}_0$ for diagonalizing its Hessian $\boldsymbol{H}(\mathbf{x}_0)$. It is natural to use $\mathbf{x}_0$ as the reference configuration. That is, project the vector $\{\mathbf{b}_j(\mathbf{x})\}$ onto the vector $\{\mathbf{b}_{0k}(\mathbf{x}_0)\}$ to define the average quantum correction factor matrix $\langle\mathbf{Q}\rangle$. The kth element of the diagonal matrix $\langle\mathbf{Q}\rangle$ is expressed as

$$\langle Q_k\rangle = \left\langle \sum_j \left|\mathbf{b}_j^T(\mathbf{x})\cdot\mathbf{b}_{0k}(\mathbf{x}_0)\right|^2 Q_j(\mathbf{x}) \right\rangle \tag{A10}$$

or

$$\langle Q_k^{-1}\rangle = \left\langle \sum_j \left|\mathbf{b}_j^T(\mathbf{x})\cdot\mathbf{b}_{0k}(\mathbf{x}_0)\right|^2 Q_j^{-1}(\mathbf{x}) \right\rangle. \tag{A11}$$

The bracket in Eqs. (A10) and (A11) represents the canonical ensemble average over $\mathbf{x}$. It is sometimes useful to take

$$\langle Q_k\rangle = \frac{1}{2}\left[\left\langle \sum_j \left|\mathbf{b}_j^T(\mathbf{x})\cdot\mathbf{b}_{0k}(\mathbf{x}_0)\right|^2 Q_j(\mathbf{x}) \right\rangle \right.$$
$$\left. + \left\langle \sum_j \left|\mathbf{b}_j^T(\mathbf{x})\cdot\mathbf{b}_{0k}(\mathbf{x}_0)\right|^2 Q_j^{-1}(\mathbf{x}) \right\rangle^{-1}\right]. \tag{A12}$$

The thermal mass matrix then becomes

$$\mathbf{M}_{therm} = \mathbf{M}^{1/2}\mathbf{T}_0\langle\mathbf{Q}\rangle\mathbf{T}_0^T\mathbf{M}^{1/2}, \tag{A13}$$

which is independent of the position $\mathbf{x}$. Evaluation of the thermal mass matrix $\mathbf{M}_{\text{therm}}$ as defined by Eqs. (A10)–(A13) does not request any specific form of the potential energy surface and takes the similar procedure as we estimate thermodynamic properties such as the kinetic energy. Apparently, Eqs. (A6) and (A13) are exact in the harmonic limit.

Using the relation

$$\frac{\left\langle \mathbf{x} - \frac{\Delta\mathbf{x}}{2}\left|e^{-\beta\hat{H}}\right|\mathbf{x} + \frac{\Delta\mathbf{x}}{2}\right\rangle}{\left\langle \mathbf{x}\left|e^{-\beta\hat{H}}\right|\mathbf{x}\right\rangle} \approx \exp\left[-\frac{\Delta\mathbf{x}^T\mathbf{M}_{therm}\Delta\mathbf{x}}{2\hbar^2\beta}\right], \tag{A14}$$

it is straightforward to follow the same procedure for the LSC-IVR/classical Wigner model as shown in Refs. 2 and 25 to express the correlation function in the Wigner phase space [i.e., obtain the function $f_{A\beta}^W(\mathbf{x},\mathbf{p})$ in Eq. (5)].

Because the normal mode frequencies for overall translational and rotational corrections of the complete molecule are very small ($|\omega_k| \sim 0$) and well separated from the high-frequency vibrational region of interest, the average quantum correction factors $\{\langle Q_k\rangle\}$ for these normal modes are set to zero in Eqs. (A10)–(A13) for accomplishing the translational and rotational corrections of real time dynamics.

Note that no translational or rotational correction is applied when using PIMD to sample the configuration of the molecule. It is necessary to align the molecular configuration $\mathbf{x}$ and the equilibrium one $\mathbf{x}_0$ before evaluating the term $\left|\mathbf{b}_j^T(\mathbf{x})\cdot\mathbf{b}_{0k}(\mathbf{x}_0)\right|^2$ for the average quantum correction factor matrix $\langle\mathbf{Q}\rangle$. The Kabsch algorithm[63–65] is employed for this purpose in the article.

[1] E. B. Wilson, Jr., J. C. Decius, and P. C. Cross, *Molecular Vibrations: The Theory of Infrared and Raman Vibrational Spectra* (Dover Publications, Inc., New York, 1980).

[2] J. Liu, W. H. Miller, G. S. Fanourgakis, S. S. Xantheas, S. Imoto, and S. Saito, J. Chem. Phys. **135**(24), 244503 (2011).

[3] M. Rossi, M. Ceriotti, and D. E. Manolopoulos, J. Chem. Phys. **140**(23), 234116 (2014).

[4] A. Witt, S. D. Ivanov, M. Shiga, H. Forbert, and D. Marx, J. Chem. Phys. **130**(19), 194510 (2009).

[5] D. Marx, M. E. Tuckerman, and G. J. Martyna, Comput. Phys. Commun. **118**(2-3), 166–184 (1999).

[6] M. Pavese, D. R. Berard, and G. A. Voth, Chem. Phys. Lett. **300**(1-2), 93–98 (1999).

[7] Y. Ohta, K. Ohta, and K. Kinugawa, J. Chem. Phys. **120**(1), 312–320 (2004).

[8] J. A. Poulsen, G. Nyman, and P. J. Rossky, Proc. Natl. Acad. Sci. U. S. A. **102**(19), 6709–6714 (2005).

[9] M. Shiga and A. Nakayama, Chem. Phys. Lett. **451**(4-6), 175–181 (2008).

[10] X. Huang, S. Habershon, and J. M. Bowman, Chem. Phys. Lett. **450**(4-6), 253–257 (2008).

[11] A. Kaczmarek, M. Shiga, and D. Marx, J. Phys. Chem. A **113**(10), 1985–1994 (2009).

[12] F. Paesani and G. A. Voth, J. Phys. Chem. B **113**(17), 5702–5719 (2009).

[13] F. Paesani, S. S. Xantheas, and G. A. Voth, J. Phys. Chem. B **113**(39), 13118–13130 (2009).

[14] J. Liu, W. H. Miller, F. Paesani, W. Zhang, and D. A. Case, J. Chem. Phys. **131**(16), 164509 (2009).

[15] S. Habershon, G. S. Fanourgakis, and D. E. Manolopoulos, J. Chem. Phys. **129**(7), 074501 (2008).

[16] S. Habershon and D. E. Manolopoulos, J. Chem. Phys. **131**(24), 244518 (2009).

[17] M. Rossi, H. Liu, F. Paesani, J. Bowman, and M. Ceriotti, J. Chem. Phys. **141**(18), 181101 (2014).

[18] M. Basire, D. Borgis, and R. Vuilleumier, Phys. Chem. Chem. Phys. **15**(30), 12591–12601 (2013).

[19] F. Calvo, V.-O. Nguyen-Thi, P. Parneix, and C. Falvo, Phys. Chem. Chem. Phys. **14**(30), 10503–10506 (2012).

[20] J. Beutier, R. Vuilleumier, S. Bonella, and G. Ciccotti, Mol. Phys. **113**(17-18), 2894–2904 (2015).

[21]H. Wang, X. Sun, and W. H. Miller, J. Chem. Phys. **108**(23), 9726–9736 (1998).

[22]X. Sun, H. Wang, and W. H. Miller, J. Chem. Phys. **109**(17), 7064–7074 (1998).

[23]Q. Shi and E. Geva, J. Phys. Chem. A **107**, 9059–9069 (2003).

[24]J. A. Poulsen, G. Nyman, and P. J. Rossky, J. Chem. Phys. **119**(23), 12179 (2003).

[25]J. Liu and W. H. Miller, J. Chem. Phys. **131**(7), 074113 (2009).

[26]W. H. Miller, J. Chem. Phys. **125**(13), 132305 (2006).

[27]J. A. Poulsen, G. Nyman, and P. J. Rossky, J. Chem. Theory Comput. **2**(6), 1482–1491 (2006).

[28]B. J. Ka, Q. Shi, and E. Geva, J. Phys. Chem. A **109**(25), 5527–5536 (2005).

[29]J. Liu, Int. J. Quantum Chem. **115**(11), 657–670 (2015).

[30]J. Cao and G. A. Voth, J. Chem. Phys. **99**(12), 10070–10073 (1993).

[31]G. A. Voth, Adv. Chem. Phys. **93**, 135 (1996).

[32]S. Jang and G. A. Voth, J. Chem. Phys. **111**, 2371–2384 (1999).

[33]T. D. Hone, P. J. Rossky, and G. A. Voth, J. Chem. Phys. **124**(15), 154103 (2006).

[34]I. R. Craig and D. E. Manolopoulos, J. Chem. Phys. **121**(8), 3368–3373 (2004).

[35]T. F. Miller III and D. E. Manolopoulos, J. Chem. Phys. **122**(18), 184503 (2005).

[36]B. J. Braams and D. E. Manolopoulos, J. Chem. Phys. **125**(12), 124105 (2006).

[37]S. Habershon, D. E. Manolopoulos, T. E. Markland, and T. F. Miller III, Annu. Rev. Phys. Chem. **64**, 387–413 (2013).

[38]S. Jang, A. V. Sinitskiy, and G. A. Voth, J. Chem. Phys. **140**(15), 154103 (2014).

[39]T. J. H. Hele, M. J. Willatt, A. Muolo, and S. C. Althorpe, J. Chem. Phys. **142**(19), 191101 (2015).

[40]We note that a typo exists in Eq. (2.6) of Ref. 14, i.e., $\hbar\beta$ was missing in the right term of Eq. (2.6). The correct equation [Eq. (1)] was in fact used in Ref. 14 though.

[41]R. Kubo, M. Toda, and N. Hashitsume, *Statistical Physics II: Nonequilibrium Statistical Mechanics*, 2nd ed. (Springer-Verlag, Heidelberg, 1991).

[42]J. Liu, J. Chem. Phys. **140**(22), 224107 (2014).

[43]J. Liu, J. Chem. Phys. **134**(19), 194110 (2011).

[44]J. Liu and W. H. Miller, J. Chem. Phys. **126**(23), 234110 (2007).

[45]J. Liu and W. H. Miller, J. Chem. Phys. **134**(10), 104101 (2011).

[46]J. Liu and W. H. Miller, J. Chem. Phys. **134**(10), 104102 (2011).

[47]E. L. Pollock and D. M. Ceperley, Phys. Rev. B **30**(5), 2555–2568 (1984).

[48]M. E. Tuckerman, B. J. Berne, G. J. Martyna, and M. L. Klein, J. Chem. Phys. **99**(4), 2796–2808 (1993).

[49]D. Chandler and P. G. Wolynes, J. Chem. Phys. **74**, 4078–4095 (1981).

[50]G. Bussi and M. Parrinello, Phys. Rev. E **75**(5), 056707 (2007).

[51]M. Ceriotti, M. Parrinello, T. E. Markland, and D. E. Manolopoulos, J. Chem. Phys. **133**(12), 124104 (2010).

[52]J. Liu, D. Li, and X. Liu, Sci. Sin. Chim. **46**, 27–37 (2016).

[53]J. Liu, X. Liu, and D. Li, "Comparison of two integrators for path integral molecular dynamics with Langevin thermostat" (unpublished).

[54]B. Leimkuhler and C. Matthews, J. Chem. Phys. **138**(17), 174102 (2013).

[55]B. Leimkuhler and C. Matthews, Appl. Math. Res. Express **1**, 34–56 (2013).

[56]H. Partridge and D. W. Schwenke, J. Chem. Phys. **106**(11), 4618–4639 (1997).

[57]S. N. Yurchenko, J. G. Zheng, H. Lin, P. Jensen, and W. Thiel, J. Chem. Phys. **123**(13), 134308 (2005).

[58]X.-G. Wang and T. Carrington, Jr., J. Chem. Phys. **141**(15), 154106 (2014).

[59]J. Shao and N. Makri, J. Phys. Chem. A **103**, 7753–7756 (1999).

[60]J. Shao and N. Makri, J. Phys. Chem. A **103**, 9479–9486 (1999).

[61]N. Makri, A. Nakayama, and N. Wright, J. Theor. Comput. Chem. **3**, 391–417 (2004).

[62]A. Nakayama and N. Makri, Proc. Natl. Acad. Sci. U. S. A. **102**(12), 4230–4234 (2005).

[63]W. Kabsch, Acta Crystallogr., Sect. A: Cryst. Phys., Diffr., Theor. Gen. Crystallogr. **A32**, 922–923 (1976).

[64]W. Kabsch, Acta Crystallogr., Sect. A: Cryst. Phys., Diffr., Theor. Gen. Crystallogr. **A34**, 827–828 (1978).

[65]See http://www.mathworks.com/matlabcentral/fileexchange/25746-kabsch-algorithm for a description of the Kabsch algorithm and for a MatLab subroutine on the algorithm.